Nanoparticle emission by electronic sputtering of CaF$_2$ single crystals

I. Alencar[a,b,*], M. Hatori[a,1], G.G. Marmitt[a], H. Trombini[a], P.L. Grande[a], J.F. Dias[a], R.M. Papaléo[b], A. Mücklich[c], W. Assmann[d], M. Toulemonde[e], C. Trautmann[f,g]

[a] Laboratório de Implantação Iônica, Universidade Federal do Rio Grande do Sul (UFRGS), Porto Alegre CEP 91501-970, Brazil
[b] Escola Politécnica, Pontifícia Universidade Católica do Rio Grande do Sul (PUCRS), Porto Alegre CEP 90619-900, Brazil
[c] Helmholtz-Zentrum Dresden-Rossendorf (HZDR), Dresden D-01328, Germany
[d] Fakultät für Physik, Ludwig-Maximilians-Universität München (LMU), Garching D-85748, Germany
[e] Centre de Recherche sur les Ions, les Matériaux et la Photonique (CIMAP), Caen F-14070, France
[f] Materialforschung, GSI Helmholtzzentrum für Schwerionenforschung, Darmstadt D-64291, Germany
[g] Fachbereich Materialwissenschaften, Technische Universität Darmstadt, Darmstadt D-64287, Germany

ARTICLE INFO

ABSTRACT

Material sputtered from CaF$_2$ single crystals by 180 MeV Au ions impinging at different incidence angles were collected on high-purity amorphous C-coated Cu grids and Si(1 0 0) wafer catcher surfaces over a broad angular range. These catcher surfaces were characterized complementary by transmission electron microscopy, atomic force microscopy and medium energy ion scattering, revealing the presence of a distribution of partially buried CaF$_2$ nanoparticles in conjunction to a thin layer of deposited CaF$_2$ material. Particle size distributions do not follow simple power laws and depend on the angles of ion incidence and particle detection. It is shown that the particle ejection is directly related to the jet-like component of sputtering, previously observed in ionic crystals, contributing significantly to the total yield. This contribution enhances as the impinging ions approach grazing incidence. Possible scenarios for the emission of particles are discussed in light of these observations.

1. Introduction

Swift heavy ions ($v_{ion} > v_{Bohr} = 2.2 \times 10^6$ m s^{-1}) impinging on solids are able to eject a very large number of particles. Such a phenomenon, denoted electronic sputtering, is a consequence of the predominant energy deposition by electronic excitation and is particularly efficient in dielectric materials [1]. Depending on the target properties, the angle of incidence and the ion energy, a total mass of the order of 10^6 u could be sputtered in a single ion impact [2–6], comprising large intact molecules, molecular fragments, clusters of atoms or atomized species. Sputtering by high-energy ions have been widely explored for thin film deposition [7] and patterning of surfaces [8,9], as well as for mass spectrometry [10–12] and molecular imaging of biological tissues [13]. It also has implications to a broad range of fields, including the evolution of planetary atmospheres and interstellar dust grains [14–17].

Electronic sputtering has often been attributed to either the evaporation/sublimation due to the transient heating following relaxation of the highly excited ion track [18] or the evaporation following diffusion of the products from self-trapped exciton decays [19,20].

However, as large thermally labile biomolecules might also be ejected intact by a swift heavy ion [21], non-thermal processes based on coherent movement of a volume of atoms (pressure waves) by a sum of impulses were proposed [22,23]. Additionally, Coulomb repulsion could be responsible for atomic motion in the highly excited ion track, but neutralization is usually too fast to allow for electronic sputtering. Nevertheless, it is argued that possible small displacements induced by such repulsions may lead to electron-lattice coupling, where highly excited states could decay non-radiatively and, consequently, cause sputtering [24]. Albeit several basic aspects of electronic sputtering have already been clarified [25,26], many mechanistic aspects are not yet well understood.

An example is the strong jet-like component of emission observed for ionic crystals [3,5]. Unusually large total yields have been reported (e.g. ~10^4 atoms per incident 210 MeV Au ion for LiF single crystals), well beyond estimations based on thermal spike calculations or contributions from elastic collisional cascade sputtering. Peaked angular distributions have been proposed in the so-called gas-flow or phase explosion models of sputtering, where local heating of a volume of the

---

* Corresponding author at: Departamento de Física, Universidade Federal de Santa Catarina (UFSC), CEP 88040-900 Florianópolis, Brazil.
E-mail address: igor.alencar@ufsc.br (I. Alencar).

[1] This work is dedicated to the memory of Masahiro Hatori, who was a young physicist pursuing a doctoral degree. He actively participated in the research group at UFRGS, where his cheerful easiness and calm propitiated an enjoyable relationship inside and outside the laboratory.

solid causes an abrupt transition to the gas phase with subsequent expansion and flow of material into the vacuum [27]. The expansion and cooling of an initially hot column of vaporized material is also expected to result in clustering of the emitted species. Indeed, clustering has been routinely evidenced in secondary ion mass spectra of several materials bombarded by swift heavy ions [28,29]. In a few cases, like in Au and Ag films [30–33], embedded Au nanoparticles [34,35], and Au nanorods [36], direct observation of sputtered material collected by catcher foils revealed the presence of a distribution of nanoparticles (NPs) much larger than typical cluster sizes seen in mass spectrometry. Such a process may also occur for bulk ionic crystals, but has not been reported so far.

The simple compositional, structural and optical properties of bulk, binary ionic crystals have attracted research interest for a long time. This is not different for radiation materials science and, in particular, for electronic sputtering investigations. By far, studies employing LiF crystals as targets are the most commonly reported. Results from Secondary Ion Mass Spectrometry (SIMS) techniques include evidence for surface metalization [37], and the determination of energy distributions for atomized [38,39] and cluster [40] species, of angular distribution for cluster species [41] and of yield dependence on energy loss for cluster species [29]. Usually, these cluster species are composed by $(LiF)_n Li^+$ with $n \leqslant 5$. Their individual yields are reported to be at least three orders of magnitude below total sputter yields, demonstrating that only a tiny fraction of the ejecta is constituted by charged species. These total sputter yields are generally determined employing the catcher technique, where high-purity surfaces are positioned at fixed distances and angles in order to collect the ejecta. Besides the aforementioned observation of preferential sputtering (the jet-like component) [3–5], charge-state effects [42], ejecta stoichiometry [43] and its energy loss dependency as well as the azimuthal symmetry [44] were throughly considered.

In this work, we provide direct experimental evidence of NP emission due to electronic sputtering of CaF_2 single crystals induced by 180 MeV Au ions. The NP size distributions vary with both angles of ion incidence and particle collection. In addition, by combining microscopy observations with ion scattering spectrometry measurements, we show that the jet-like component of sputtering is essentially formed by these NPs, contributing significantly to the total yield.

2. Materials and methods

2.1. Samples and irradiations

High-purity CaF_2 single crystals were annealed for one hour under an inert atmosphere and freshly cleaved just before the irradiations. The CaF_2 cleaved crystals were placed as targets in a custom-built, movable sample holder. Fig. 1 shows a sketch of the geometry as well as a photography of the sample holder for the sputtering experiments. Across the target, a supporting arc (1.9 cm radius) was covered by

(a) sketch

(b) movable sample holder
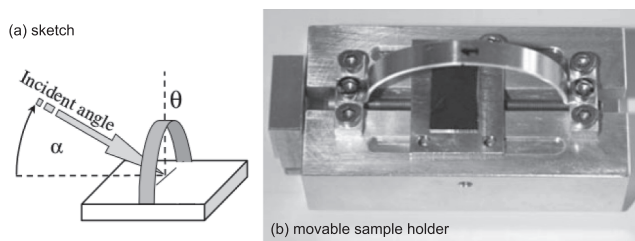
Fig. 1. Setup for the sputtering experiment. (a) Sketch of the experimental geometry. The vertical dashed line denotes $\theta = 0°$ of the angular distribution for ejecta collected on catchers covering the arc-shaped support. (b) Photography of the custom-built, movable sample holder including the supporting arc used to dispose the catchers.

several catchers at various collection angles ($-60 < \theta < 70°$) from the target normal.

Au ions at the energy of 180 MeV were delivered from a 12 MV tandem accelerator (MLL, Garching, Germany) after passing through a thin carbon stripper foil (10 $\mu g\ cm^{-2}$) placed 10 cm before the target. The stripper foil is employed simultaneously to promote charge equilibrium of the ions and to monitor the ion flux using the current induced in this foil after calibration with a Faraday cup placed downstream. Irradiations were performed at room temperature under a pressure smaller than 10^{-5} Pa. Three different angles of incidence α (20, 45 and 70°) with beam spot radii ranging between 0.9 and 1.5 mm were selected. According to the SRIM-2012.01 code [45], the predominant (>99%) electronic energy loss at the target surface is 23.4 keV nm^{-1}. In order to avoid significant surface corrugation or target modification by the beam, as previously reported for swift heavy ion irradiations [46–48], up to 90 different spots were irradiated on the movable CaF_2 target, each with a fluence below 3×10^{11} Au ions cm^{-2}. Ejecta were collected on small pieces of clean Si(1 0 0) wafers or amorphous C-coated Cu-grids, arranged at alternating positions on the arc with angular steps of roughly 11°. Hereafter, such pieces are referred to as Si and C catchers.

2.2. Characterization techniques

Transmission Electron Microscopy (TEM) was carried out on the C catchers using a FEI Titan 80–300 instrument (HZDR, Dresden, Germany) in bright-field contrast mode.

Atomic Force Microscopy (AFM) was performed on the Si catchers by a Bruker Dimension Icon PT instrument (PUCRS, Porto Alegre, Brazil) using the tapping mode at ambient conditions. For the measurements, standard Si cantilevers (Bruker and Nanosensors) of 125 μm length, 30–35 μm width and 2–4 μm thickness with pyramidal probes (tips) of 10–15 μm height, 10° half cone angle and better than 10 nm radii at the apex were used to record topographs of 256 scan lines per frame with 1 kHz scanning rate. Surface topographs were analyzed with the Gwyddion software [49] using a three-step procedure. In the first step, topographs were treated with four tools: level data by mean plane subtraction; correct lines by matching height median; correct horizontal scars (strokes); and shift minimum data value to zero. In the second step, a height threshold above the maximum found for the substrate was applied as a discriminator (mask). In the third step, the watershed algorithm [50,51] was used for the segmentation of particle clusters. This algorithm finds local minima within each masked region in order to distinguish agglomerated particles, allowing the height determination of each particle individually. These heights must, finally, be corrected by subtraction of the substrate mean height.

Medium Energy Ion Scattering (MEIS) spectra of the Si catchers were acquired employing 100 keV He^+ ions delivered from a 500 kV electrostatic accelerator (UFRGS, Porto Alegre, Brazil). During the measurements, backscattered ions were collected for scattering angles φ ranging from 108 to 132°. A set of two microchannel plates coupled to a position-sensitive detector allowed energy-angle heat-maps with channel bins of roughly 0.1 keV and angular acceptance of 0.08° to be recorded using a toroidal electrostatic analyzer [52]. The considerable energy resolving-power of MEIS makes it a very sensitive probe at the near surface, allowing compositional and structural characterization of materials at the nanometer scale [53]. For each catcher, a total charge of less than 5 μC (equivalent to a fluence of 4×10^{15} He^+ ions cm^{-2}) was accumulated employing ion currents smaller than 15 nA (equivalent to a flux of 1.2×10^{13} He^+ ions $cm^{-2}\ s^{-1}$) at a millimeter-sized single spot. Measurements from different spots on the same catcher were summed up for analysis. For analysis of MEIS spectra, simulations were performed with the PowerMEIS3 code [54,55], developed to simulate ion scattering spectra of surfaces with morphological and compositional parameters adjustable at the nanometer scale. In such simulations, different compounds can be attributed for each volume

element dV of the sample under study, allowing the construction of complex structures using the voxel representation. The scattering yield dH_{ij} detected at energy E_{out} caused by an elastic collision with the i-th element in a volume situated at the j-th position of the sample can be written as [56]:

$$dH_{ij} = x_i Q \Omega \sigma_i(E_1, \varphi) f(E_{out} - E_2) DF(E_{out}) N_j dV \qquad (1)$$

with $\quad E_1 = E_0 - \Delta E_{in} \quad$ and $\quad E_2 = K_i(\varphi)E_1 - \Delta E_{out}$

where x_i is the atomic fraction of the i-th element, Q the fluence of incident He$^+$ ions, Ω the detector solid angle, σ_i the differential scattering cross section for the i-th element, f the energy loss distribution, D the channel bin, F the neutralization probability correction, and N_j the atomic density at the j-th position. φ is the scattering angle, E_0 the incident He$^+$ ion energy, E_1 (E_2) the energy immediately before (after) the scattering collision, K_i the kinematic factor of the i-th element, and ΔE_{in} (ΔE_{out}) the energy loss across the incoming (outgoing) trajectory. The differential scattering cross section is determined from the Molière potential [57]. The energy loss distribution is caused by fluctuations in the interactions with target atoms and by the resolution of the detection system. For Rutherford Backscattering Spectrometry (RBS), a Gaussian function suffices to describe the energy loss distribution as the large number of inelastic interactions cannot be resolved. For MEIS, in contrast, the implications caused by a small number of such interactions need to be taken into account [58]. The simple analytical form of the Exponentially Modified Gaussian (EMG) is therefore applied to the energy loss distribution [59]. The neutralization probability correction is evaluated from data tables [60] and the energy loss is calculated from the SRIM library [45]. All simulations were performed with 5×10^7 interactions, 0.3 keV channel bin, 650 eV energy resolution, and 4° angular acceptance at the chosen scattering angle. For each element, all stable isotopes were considered.

3. Results and analyses

### 3.1. Transmission electron microscopy

TEM micrographs of the C catchers show the presence of NPs with circular cross-section (Fig. 2, insets). Size distribution and areal density depend on the angles of ion incidence and particle collection. Relatively large NPs ($\geqslant$15 nm diameter) are seen, even when areal densities are small. In addition, the size distributions appear to be Gaussian in shape, contrasting the simple power law found for metallic targets [33,34,36,61,62]. Each distribution is, in fact, well described by a sum of two Gaussian functions (Fig. 2, main plots). Mean NP diameter averaged from all combination of angles are 4.1 ± 0.8 and 9.0 ± 0.8 nm.

Individual particles were imaged by High-Resolution TEM (HRTEM). A typical NP exhibiting periodic arrangement and the aforementioned circular cross-section is shown in Fig. 3(a). The observation of large-sized particles ($\geqslant$15 nm diameter) allows Fast Fourier Transform (FFT) analysis of a selected area enclosing each of them to be performed. From inspection of the reciprocal space, it is possible to determine the NP planar distance (d-spacing), as illustrated in Fig. 3(b). The results (0.313–0.319 nm) are in excellent agreement to what is expected from CaF$_2$ crystals (0.318 nm), giving evidence for the emission of crystalline, stoichiometric CaF$_2$ NP.

3.2. Atomic force microscopy

Height distributions of NPs determined from analyses of AFM topographs are also bimodal and characterized by mean heights of 2.0 ± 0.4 and 4.7 ± 0.7 nm (Fig. 4). These height values are about half of the NP diameters extracted from examination of TEM micrographs, which is consistent with particles of spherical shape.

Sphericity is also deduced from the analysis of the frequency distribution of height values obtained from AFM topographs. For this
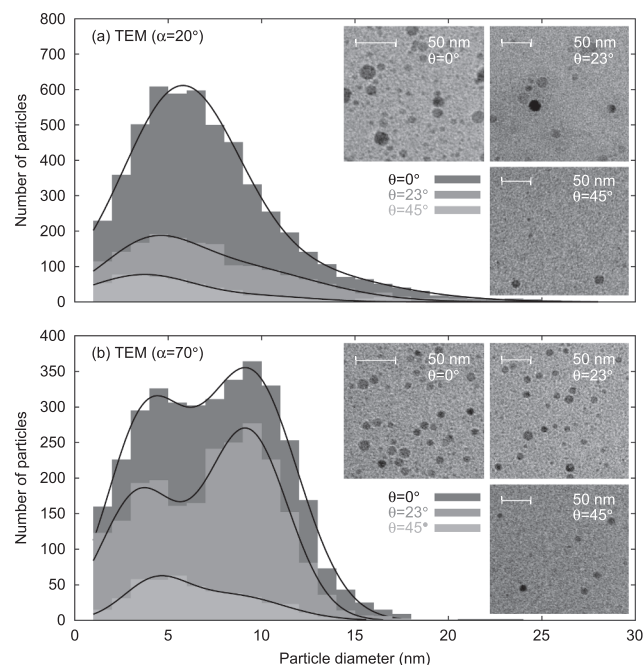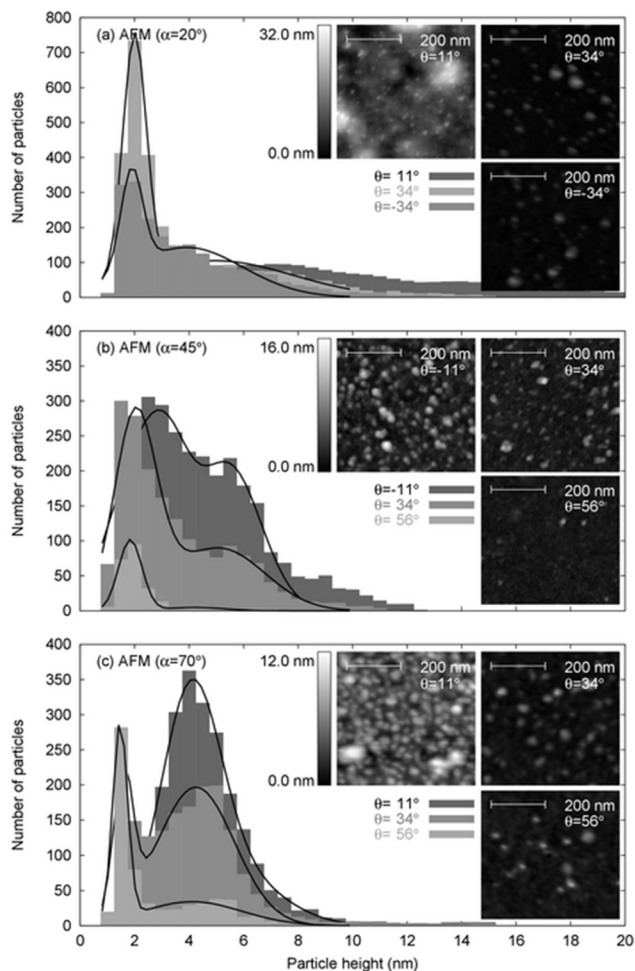

Fig. 2. Diameter histograms. Particles collected on amorphous C-coated Cu-grid catchers placed at different detection angles θ. TEM micrographs totalizing a scan area of 1.25 μm^2. (a–b) Ion incidence at $\alpha = 20$ and 70°, respectively, with cumulative total fluences of 2.5 and 3.0×10^{12} Au ions cm^{-2} for 8 and 90 irradiation spots. Solid lines are fits with a sum of two Gaussian functions. Insets show representative micrographs.
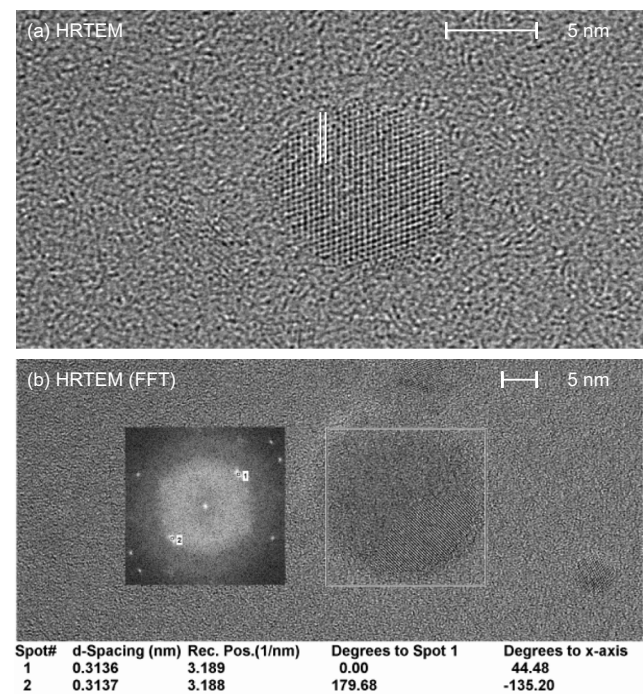

Fig. 3. High-Resolution TEM. (a) Real space image of circular NP with periodic array. Parallel (vertical) white solid lines highlight the periodicity. (b) Real space image and reciprocal space analyses by Fast Fourier Transform (FFT) in the squared, selected area containing a CaF$_2$ nanocrystal with circular cross-section.

Spot#	d-Spacing (nm)	Rec. Pos.(1/nm)	Degrees to Spot 1	Degrees to x-axis
1	0.3136	3.189	0.00	44.48
2	0.3137	3.188	179.68	-135.20

purpose, NP metrology was performed on a topograph containing the smallest amount of particles (i.e. the case of ion incidence at $\alpha = 45°$ and detection at $\theta = 56°$). Each point of the 256 per 256 frame was considered as a pixel with a height value attributed to it. The resulting

Fig. 4. Height histograms. Particles collected on Si(1 0 0) wafer catchers placed at different detection angles θ. AFM topographs totalizing a scan area of 8.25 μm^2 except for $\alpha = 20°$ and $\theta = 11°$ (9.50 μm^2), $\alpha = 45°$ and (4.25 μm^2), and $\alpha = 70°$ and $\theta = 11°$ (12.45 μm^2). (a–c) Ion incidence at $\alpha = 20, 45$ and $70°$, respectively, with cumulative total fluences of 2.5, 2.2 and 3.0×10^{12} Au ions cm^{-2} for 8, 58 and 90 irradiation spots. Solid lines represent fits with a sum of two Gaussian functions. Insets show representative topographs.
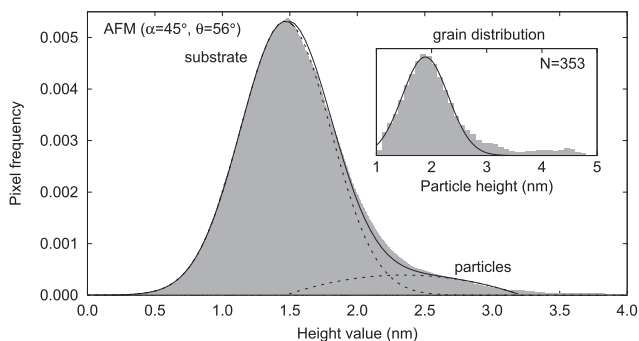
Fig. 5. Particle metrology. Pixel frequency of height values extracted from an AFM topograph comprised of single particles collected on a Si(1 0 0) wafer catcher (i.e. the case of ion incidence at $\alpha = 45°$ and detection at $\theta = 56°$, with a cumulative total fluence of 2.2×10^{12} Au ions cm^{-2} for 58 irradiation spots). The solid line represents the fit with a sum of a Gaussian function and a parabolic function. Inset shows the height distribution of particles, where the solid line represents another fit with a Gaussian function.

distribution of pixel frequencies is shown as a histogram in Fig. 5 (main plot). Due to the finite curvature radius of the tip and the roughness of the substrate, the pixel frequency distribution of height values for the
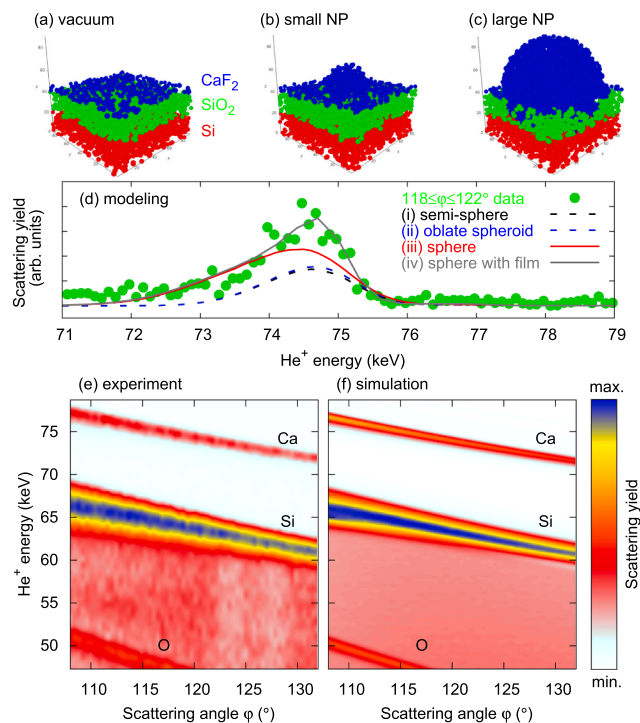
Fig. 6. MEIS analyses. Spectra recorded for Si(1 0 0) wafer catchers. (a–c) Voxel representation of the building units (cubic boxes with 9.0 nm edges) for the best fitting model considering partially buried NPs, a thin film and a native oxide layer. (d) Scattering yield integrated in the angular range $118 \leqslant \varphi \leqslant 122°$ for ion incidence at $\alpha = 20°$ (cumulative total fluence of 2.5×10^{12} Au ions cm^{-2} for 8 irradiation spots) and detection at $\theta = 11°$. Lines denote simulations performed with different particle shapes: (i) semi-sphere; (ii) oblate spheroid; (iii) partially buried sphere; and (iv) partially buried sphere with a thin film and a native oxide layer. (e–f) Experimental and simulated, employing case (iv), energy-angle map for this same catcher, respectively.

case of isolated, spherical particles can be described as a Gaussian function (generated by the substrate) added to a parabolic function of the mean NP height [63]. This description is illustrated by the solid line in the main plot of Fig. 5, while the inset presents the NP distribution of height values fitted with a single Gaussian function. The excellent agreement of the pixel distribution with the parabolic function is a strong evidence for the sphericity of the particles on a slightly rough substrate.

3.3. Medium energy ion scattering

MEIS spectra of Si catchers analyzed by Monte Carlo simulations provide further information on the arrangement of the sputtered material on their surfaces. Unfortunately, due to the difference in the kinematic factors, the scattering yield of F species seems to be hindered by the Si substrate in the spectra and the analysis proceed considering only the scattering yield of Ca species. Simulations were performed modeling the Si catcher surface using building units consisting of cubic boxes (9.0 nm edges) filled with voxels of different compounds (CaF$_2$, Si, SiO$_2$ native wafer oxide, and vacuum), as exemplified in Fig. 6(a)–(c). As a first approximation, we consider the wafer to be composed of pure Si, occupying the lower half of the cubic units forming the catcher, and that NPs of a given shape are placed either on top or partially embedded on it. Tested shapes include semi-sphere, oblate spheroid, and partially buried sphere. For each shape, three different building units are constructed: one type contains no particle, while the other two types are filled with a single particle of the desired shape where its size corresponds to one of the mean values found from the bimodal distributions. The building units forming the catcher

surface are distributed attributing a probability factor p to each type of cubic box, according to the AFM height distributions. For example, in the case of ion incidence at $\alpha = 20°$ and detection at $\theta = 11°$, areal densities of 6.9 and 1.9×10^{11} NPs cm^{-2} were observed for particle heights distributions centered at 2.0 and 4.5 nm, respectively, corresponding to a probability factor of 56.0 and 15.6% (the remaining 28.4% is attributed to the building unit with no particle). The simulations show the partially-buried-sphere model to provide the best match (in particular, the long tail of the scattering yield for the Ca signal observed between 72–74 keV) with the experimental data, as illustrated in Fig. 6(d). Final refinement of the model for ion scattering simulation incorporates the SiO$_2$ native oxide layer and the presence of CaF$_2$ deposited thin films. From the scattering signal of O species, a 3.0 nm thick layer of the native oxide is fitted. Deposited CaF$_2$ thin films ranging from 0.3 to 0.9 nm are determined from the spectra recorded for the Si catchers placed at different collection angles for each angle of ion incidence. In this way, excellent agreement between experiments and simulations is found. A typical result is presented in Fig. 6(d)–(f).

Possible degradation of the sample caused by irradiations with the He$^+$ beam was also verified. Spectra obtained for different charge accumulations in a single spot are presented in Fig. 7(a), where significant variations in the scattering yield are definitely not observed. It is also worth noting that the fitting procedure was not influenced by the quasi-channeling condition (in the Si wafer) employed during the measurements. The capability of the voxel representation in describing complex structures allows the utilization of several layers to build the Si catcher, where a different normalization factor can be attributed to the scattering yield for each of these layers. A comparison between simulations with the same description parameters for the Si catcher and measurements performed for the case of ion incidence at $\alpha = 20°$ and detection at $\theta = 11°$ with quasi-random and quasi-channeling conditions is shown in Fig. 7(b).
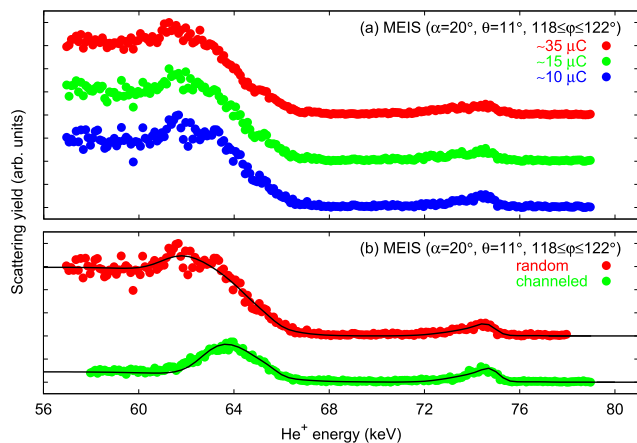
Fig. 7. Charge accumulation and channeling effects. MEIS spectra integrated in the angular interval of $118 \leqslant \varphi \leqslant 122°$ for the case of ion incidence at $\alpha = 20°$ (cumulative total fluence of 2.5×10^{12} Au ions cm^{-2} for 8 irradiation spots) and detection at $\theta = 11°$. (a) Spectra recorded at a single spot for different charge accumulations: 10, 15 and 35 μC in blue, green and red filled circles, respectively. For each charge accumulation, the spectrum is normalized to its scattering yield maximum (corresponding to five tick marks on the ordinate axis) and shifted vertically for clarity. The zero baseline level coincides with the scattering yield for energies higher than 76 keV. (b) Experimental and simulated spectra for quasi-random and quasi-channeling conditions represented by red and green filled circles and black solid lines, respectively. Experimental spectra are normalized to the scattering yield maximum observed for the quasi-random condition (corresponding to five tick marks on the ordinate axis) and shifted vertically for clarity. The zero baseline level coincides with the scattering yield for energies higher than 76 keV. (For interpretation of the references to colour in this figure legend, the reader is referred to the web version of this article.)
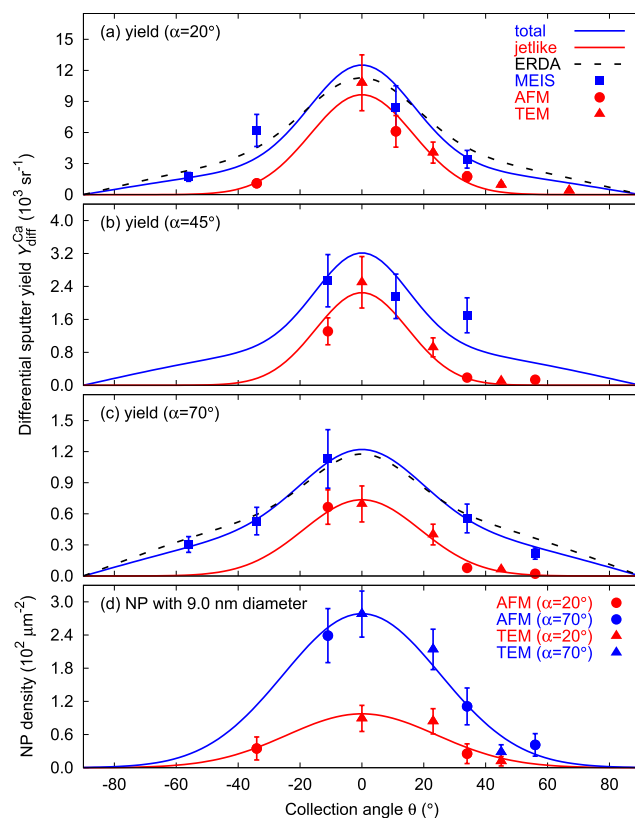
Fig. 8. Differential sputter yield and NP density. Dependence on the collection angle θ. (a–c) Differential Ca sputter yield obtained from TEM (red filled triangles), AFM (red filled circles) and MEIS (blue filled squares) analyses at incidence angles of $\alpha = 20$, 45 and 70°, respectively. Red and blue solid lines represent fits with a Gaussian function and Eq. (4), respectively, while the black dashed lines show previous ERDA results [43]. (d) Density distribution of 9.0 nm diameter NPs centered at the target normal. (For interpretation of the references to colour in this figure legend, the reader is referred to the web version of this article.)

3.4. Differential and total sputter yields

The differential sputter yield $Y_{\mathrm{diff}}^{\mathrm{Ca}}$ can be determined from the number density of collected Ca atoms N_{Ca} for each combination of angles for ion incidence α and ejecta detection θ. N_{Ca} is computed directly from integration of the Ca signal in MEIS. As mentioned previously, scattering yields for F species were not clearly identified. The differential sputter yield $Y_{\mathrm{diff}}^{\mathrm{Ca}}$ is finally obtained by:

$$Y_{\mathrm{diff}}^{\mathrm{Ca}} = \frac{s \, N_{\mathrm{Ca}} \, d_{\mathrm{catcher}}^2}{N_{\mathrm{ions}}} \tag{2}$$

where s is the sticking coefficient (hereafter assumed to be unity), d_{catcher} the distance between the catcher and target surfaces (1.9 cm) and N_{ions} the total number of incident ions (1.4–6.7×10^{12} ions, depending on the incidence angle α). The results are shown in Fig. 8(a)–(c) together with the NP differential sputter yield derived from Eq. (2) applied to number density for TEM and AFM size distributions assuming spherical particles:

$$N_{\mathrm{Ca}}^{\mathrm{NP}} = \sum_{R_{\mathrm{NP},i}=R_{\mathrm{NP,min}}}^{R_{\mathrm{Np,max}}} \frac{4\pi \, n_i \, R_{\mathrm{NP},i}^3 \, N_{\mathrm{A}}}{V_{\mathrm{m}}} \tag{3}$$

where n_i is the number of NP collected with radius $R_{\mathrm{NP},i}$, N_{A} the Avogadro number, and V_{m} the molar volume. The summation runs from the minimum to the maximal NP radii observed. Angular distributions deduced from analyses of TEM and AFM data are in excellent agreement, despite the use of different catcher materials. The dependence of
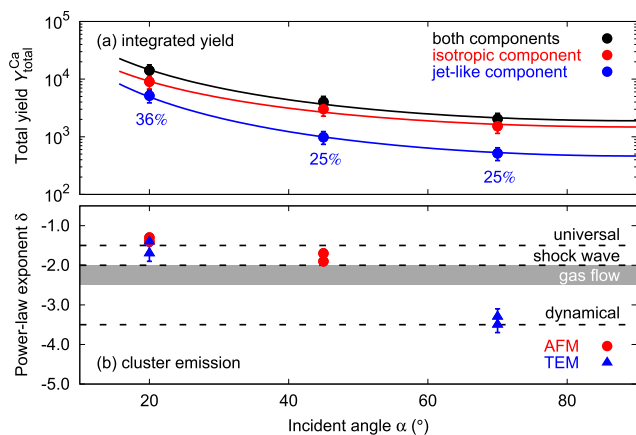
Fig. 9. Total yield and power-law exponent. Dependence on the incidence angle α. (a) Total sputter Ca yield for jet-like, isotropic and the sum of both components in black, red and blue filled circles, respectively. Solid lines are fits with Eq. (5). The contributions from the jet-like component are denoted by percentages. (b) Power-law exponent for large cluster emission. Predictions by different mechanisms are indicated horizontally. (For interpretation of the references to colour in this figure legend, the reader is referred to the web version of this article.)

$Y_{\text{diff}}^{\text{Ca}}$ on θ can be written as [3,5]:

$$Y_{\text{diff}}^{\text{Ca}}(\theta) = A\cos\theta + B\,e^{-\theta^2/2\sigma^2} \tag{4}$$

where A (B) is the weighting factor for the isotropic (jet-like) component of sputtering and σ the peak width of the jet. These parameters were obtained from the fit of Eq. (4) to the experimental data points from TEM, AFM and MEIS analyses. The jet component was fitted exclusively to TEM and AFM results, while the isotropic weighting factor was the only free parameter to fit MEIS results. The outcome is illustrated in Fig. 8(a)–(c) as red and blue solid lines, respectively. The difference between the results from analyses of TEM and AFM data to those extracted from MEIS spectra stems from the inclusion of a thin layer, attributed to the isotropic sputtering component.

The total sputter yield $Y_{\text{total}}^{\text{Ca}}$ was then estimated by integration of Eq. (4) for each incidence angle α. The result is presented in Fig. 9(a), where a steady decrease of $Y_{\text{total}}^{\text{Ca}}$ with increasing α is observed. The yield variation as a function of incidence angle can be described by:

$$Y_{\text{total}}(\alpha) = Y_{\text{total}}(90°)(\sin\alpha)^{-n} \tag{5}$$

where $\alpha = 90°$ is a normalization angle representing perpendicular ion incidence, chosen for comparison purposes with numerical predictions, and n an empirical parameter, varying between 1.7–2.2 in agreement with previous observations in a variety of materials [5].

4. Discussion

It is clearly seen that the concentration of NPs has a strong dependence on the detection angle θ for a given incidence angle α. Both diameter and height distributions show larger areal densities at angles close to the normal and these densities steeply decrease for off-normal angles. This is illustrated in Fig. 8(d) for NPs with 9.0 ± 0.5 nm diameter. As the jet-like component in sputtering of ionic crystals is preferentially oriented along the target normal [3,5], similarly to the differential Ca sputter yield presented in this work, there is clear evidence that NP emission is related to the jet. This is also consistent with previous findings that this component originates from deeper layers (effective depth ranging from 130 to 170 nm) [42], as larger amounts of material are involved.

The differential NP sputter yield $Y_{\text{diff}}^{\text{Ca}}$ was determined assuming stoichiometric emission of Ca atoms from the CaF_2 lattice [47,64]. Recent, angular-resolved investigation of catcher surfaces by Elastic

Recoil Detection Analyses (ERDA) from sputtering experiments of single CaF_2 crystals [43] showed that the F/Ca ratio is indeed stoichiometric at collection angles close to the target normal (where the sputter yield contribution from NPs is dominant), but at large detection angles it is close to unity (where the sputter yield contribution from NPs vanishes). The ERDA results for the differential sputter yield of Ca species are included in Fig. 8(a) and (c) for comparison to our data. Stoichiometric emission is also supported by the observation of CaF_2 single crystals at the C catcher employing HRTEM (Fig. 3). Furthermore, in both CaF_2 and Ca solids, the Ca atoms form a face-centered cubic structure with a small displacement of $\Delta a \approx 0.01$ nm. Even if the collected NPs were composed of pure metallic Ca, because of this similarity between the crystal structures of pure Ca and the Ca sublattice in CaF_2, the difference in yield would be at most 6%, which is smaller than the observed reproducibility of ~15% for sputtering experiments in metallic targets [65] and ~20% in alkali halides [44]. For the evaluation of differential sputter yields, it was also assumed a sticking coefficient equal to unity. The proper conversion of number density into differential sputter yield requires precise knowledge of this sticking coefficient, see Eq. (2). Recently, a sticking coefficient of 0.74 with an error of 25% was found for Cu catcher foils employed during electronic sputtering of LiF crystals [44]. This value is close enough to unity and, more importantly, the precise value of the sticking coefficient does not alter the main conclusions presented in this work.

In regard to the angular dependence of the differential sputter yield, peaked distributions were observed in experiments applying laser and electron desorption, where defect diffusion [66] or Knudsen layer formation (i.e. the regime where collisions occur in a dense gas phase near the desorbing surface) [67] have been invoked. Both these processes, nevertheless, do not seem to apply for electronic sputtering. Diffusion implies non-stoichiometric emission, whereas the jet-like component seems to be stoichiometric as discussed above. A Knudsen layer requires adiabatic expansion of a gas phase and the subsequent clustering of particles. At the typical apparent temperatures involved (between 1000 and 45000 K [68]), the kinetic energies of the particles emitted are too low (up to a few eV) to account for partially buried NPs. Additionally, inelastic Thermal Spike (iTS) calculations are not able to reproduce the large total sputter yields observed [5]. From the suitable set of iTS parameters that describes ion track radii in CaF_2 [69], the total yield calculated at 23.4 keV nm^{-1} for 1 MeV u^{-1} is only ~50 atoms per incident ion. This number is two orders of magnitude lower than the total yield estimated from our experimental results at the normalization angle of $\alpha = 90°$ (perpendicular ion incidence). Other possible processes for electronic sputtering include Coulomb explosion and exciton models. Following a Coulomb explosion, ejection of charged material would be expected, but, as previously mentioned, the yields determined for such charged ejecta detected in SIMS experiments represent an insignificant fraction of the total sputter yields [29]. Consequently, the Coulomb explosion mechanism is also not able to explain the huge sputter yields observed. Concerning exciton mechanisms, single (individual) excitation is expected at low energies and it implies on non-stoichiometric emission (e.g. section 9.2 of Ref. [20]) as well as a linear dependence on energy loss [14]. Such a linear relation is in contrast to the experimental findings of a power law dependency with an exponent ~4 [4,5,44]. Albeit such an exponent excludes the single excitation mechanism, multi-excitonic mechanisms [70] cannot be ruled out. In fact, total sputter yields in ionic crystals seem to match the upper-limit, forth-power dependency on band gap for a given energy loss [71]. Nevertheless, this mechanism does not predict the formation of NPs.

The association of the total yield to the number of atoms in the emitted particles has been frequently correlated to possible mechanisms of NP formation (clustering) employing the results from a power-law description ($Y \propto N_{\text{atoms}}^{\delta}$) [31–36, 61,62]. Such clustering models include steady-state solutions for (size independent) universal aggregation ($\delta = -3/2$) [34] and (size dependent evaporation rate) dynamical aggregation ($\delta = -7/2$) [34], shock waves ($\delta = -2$) [72] and gas flow
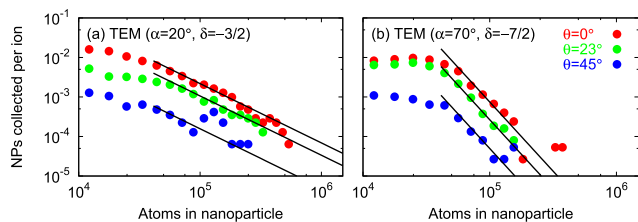
Fig. 10. Power law. Asymptotic behavior of the number of particles collected on amorphous C-coated Cu-grid catchers per incident ion (cluster yield). (a–b) Dependence on the number of atoms in the emitted particles for angles of ion incidence α = 20 and 70°, respectively. Lines are guides to the eye showing power laws with different exponents δ.

($\delta = -2$ to $-5/2$) [73]. Despite the dramatic physical dissimilarity among the models, their predictions are not too different. In our experiments, however, the size distributions strongly deviate from a simple power law. In fact, unimodal [32,35] and bimodal [31] distributions of particle size have been previously reported for sputtering of dispersed or implanted Au NPs. The vindication of the size distribution of these nanoscaled targets before irradiation as the origin of the modal distribution is clearly not valid for bulk materials, but particle fragmentation might be associated to the observation of a bimodal distribution. Similar to these previous works, the asymptotic behavior of large NPs was considered for the fit with power laws. Typical behavior is illustrated in Fig. 10. The exponent δ clearly depends on the angle of ion incidence α, increasing as the swift heavy ions are impinging at larger off-normal angles, as presented in Fig. 9(b). It is reasonable that the mechanism responsible for NP formation changes as greater amounts of energy are transferred closer to the target surface. Indeed, a shock wave mechanism has been proposed for the Au "dust off", i.e. surface removal of intact islands and film pieces, from LiF crystals at the end of the surface track, where the incident ions are penetrating subsurface layers [30].

Lastly, the total yields (each component and their sum) have an unequivocal dependence on the angle of ion incidence α, as shown in Fig. 9(a). The yield enhancement at larger off-normal angles of ion incidence is a consequence of an effective depth for energy deposition. It predicts that the ion path length for the deposition of energy varies as an inverse sine function of the angle of ion incidence α. This is a smoother function than the inverse oversine functions obtained from fits of the experimental data. Within this effective depth, the energy deposition may cause the formation of a single protrusion accompanied by a series of hillocks, as it is clearly observed for grazing incidence [74]. Increments in the energy available in the effective depth would explain the increasing contribution of the jet-like component to the total sputtering yield at larger off-normal angles of ion incidence. In fact, by integration of the angular distribution of collected NPs, it is possible to estimate the total NP density and compare the results with the total ion fluences. Roughly, fivefold more NPs are observed than the number of ions impinging on the CaF_2 crystal targets. If the bimodal distribution is caused by particle fragmentation, as suggested above, the number of NPs emitted would be reduced and a relation closer to one-to-one between NP detection and hillock formation may be verified. This would be consistent with a shock wave model for particle emission [72]. Additionally, within this scenario, the observation of crystalline hillocks with a mean diameter of 10.8 ± 1.3 nm [75] gives full support to the emission of crystalline NPs with a mean diameter around 9.0 nm.

5. Summary and conclusions

Despite electronic sputtering has implications to a broad range of research fields, both fundamental and applied, the processes involved are still open to debate. In the long-standing quest for the origin of the high sputter yields observed resides a mechanistic understanding of the phenomenon. Such a task would only be accomplished when robust sets of data are available. Here, new insights are given through a comprehensive characterization of the ejecta released during electronic sputtering of CaF_2 single crystals. A pronounced NP emission from bulk crystals is demonstrated, which is correlated to the jet-like component of sputtering. We show that the collected NPs are spherical in shape and partially buried in an outer, oxidized layer of the Si catchers. This partially buried scenario corresponds to the high energy that NPs are emitted. Despite the mechanism responsible for particle emission might depend on the angle of ion incidence, processes involving only diffusion of defects, Knudsen layers, thermal spikes, Coulomb explosion or single exciton do not account for the presented data. Moreover, larger amounts of energy deposited in an effective depth closer to the target surface may enhance the particle contribution to the total sputtering.

CRediT authorship contribution statement

I. Alencar: Conceptualization, Methodology, Validation, Formal analysis, Investigation, Writing - original draft, Writing - review & editing, Visualization. **M. Hatori:** Formal analysis. **G.G. Marmitt:** Methodology, Software. **H. Trombini:** Formal analysis, Investigation. **P.L. Grande:** Conceptualization, Methodology, Validation, Resources, Funding acquisition. **J.F. Dias:** Formal analysis, Resources, Funding acquisition. **R.M. Papaléo:** Conceptualization, Formal analysis, Resources, Writing - review & editing, Funding acquisition. **A. Mücklich:** Formal analysis, Investigation, Resources. **W. Assmann:** Conceptualization, Methodology, Validation, Resources, Writing - review & editing. **M. Toulemonde:** Conceptualization, Methodology, Validation, Resources, Writing - review & editing. **C. Trautmann:** Conceptualization, Methodology, Validation, Resources, Writing - review & editing.

Declaration of Competing Interest

The authors declare that they have no known competing financial interests or personal relationships that could have appeared to influence the work reported in this paper.

Acknowledgements

References

[1] R.D. Macfarlane, D.F. Torgerson, Science 191 (1976) 920–925.
[2] J. Eriksson, P. Demirev, R.M.P.P. Håkansson, B.U.R. Sundqvist, Phys. Rev. B 54 (1996) 15025–15033.
[3] M. Toulemonde, W. Assmann, C. Trautmann, F. Grüner, Phys. Rev. Lett. 88 (2002) 057602.
[4] M. Toulemonde, W. Assmann, C. Trautmann, F. Grüner, H.D. Mieskes, H. Kucal, Z.G. Wang, Nucl. Instr. Meth. B 212 (2003) 346–357.
[5] W. Assmann, M. Toulemonde, C. Trautmann, Topics Appl. Phys. 110 (2007) 401–450.
[6] R.M. Papaléo, R. Thomaz, L.I. Gutierres, V.M. de Menezes, D. Severin, C. Trautmann, D. Tramontina, E.M. Bringa, P.L. Grande, Phys. Rev. Lett. 114 (2015) 118302.
[7] D. Manova, J.W. Gerlach, S. Mändl, Materials 3 (2010) 4109–4141.
[8] F. Watt, A.A. Bettiol, J.A. van Kan, E.J. Teo, M.B.H. Breese, Int. J. Nanosci. 4 (2005) 269–286.
[9] L. Bruchhaus, P. Marazov, L. Bischoff, J. Gierak, A.D. Wieck, H. Hövel, Appl. Phys. Rev. 4 (2017) 011302.
[10] P.A. Demirev, Mass Spectrom. Rev. 14 (1995) 279–308.
[11] L. Jeromel, Z. Siketić, N.O. Potočnik, P. Vavpetič, Z. Rupnik, K. Bučar, P. Pelicon, Nucl. Instr. Meth. B 332 (2014) 22–27.
[12] L. Breuer, P. Ernst, M. Herder, F. Meinerzhagen, M. Bender, D. Severin, A. Wucher,

       Nucl. Instr. Meth. B 435 (2018) 101–110.

[13] T. Seki, Y. Wakamatsu, S. Nakagawa, T. Aoki, A. Ishihara, J. Matsuo, Nucl. Instr. Meth. B 332 (2014) 326–329.

[14] R.E. Johnson, Rev. Mod. Phys. 68 (1996) 305–312.

[15] E.M. Bringa, S.O. Kucheyev, M.J. Loeffler, R.A. Baragiola, A.G.G.M. Tielens, Z.R. Dai, G. Graham, S. Bajt, J.P. Bradley, C.A. Dukes, T.E. Felter, D.F. Torres, W. van Breugel, Astrophys. J. 662 (2007) 372–378.

[16] E. Dartois, M. Chabot, T. Pino, M. Godard, D. Severin, M. Bender, C. Trautmann, Astron. Astrophys. 599 (2017) A130.

[17] H. Rothard, A. Domaracka, Ph. Boduch, M.E. Palumbo, G. Strazzulla, E.F. da Silveira, E. Dartois, J. Phys. B: At. Mol. Opt. Phys. 50 (2017) 062001.

[18] R.R. Lucchese, J. Phys. C: Solid State Phys. 86 (1987) 443–453.

[19] M. Szymoński, Mat. Fys. Medd. K. Dan. Vidensk. Selsk. 43 (1993) 495–526.

[20] N. Itoh, A.M. Stoneham, Materials Modification by Electronic Excitation, Cambridge University Press, 2001.

[21] R.E. Johnson, Int. J. Mass Spectrom. Ion Proc. 78 (1987) 357–392.

[22] R.E. Johnson, B.U.R. Sundqvist, A. Hedin, D. Fenyö, Phys. Rev. B 40 (1989) 49–53.

[23] E.M. Bringa, R.E. Johnson, R.M. Papaléo, Phys. Rev. B 65 (2002) 094113.

[24] N. Matsunami, S. Okayasu, M. Sataka, Nucl. Instr. Meth. B 435 (2018) 142–145.

[25] G. Betz, K. Wien, Int. J. Mass Spectrom. Ion Proc. 140 (1994) 1–110.

[26] H.M. Urbassek, C. Anders, Y. Rosandi, Nucl. Instr. Meth. B 269 (2011) 947–954.

[27] H.M. Urbassek, H. Kafemann, R.E. Johnson, Phys. Rev. B 49 (1994) 786–795.

[28] G. Brinkmalm, P. Demirev, D. Fenyö, Håkansson, J. Kopniczky, B.U.R. Sundqvist, Phys. Rev. B 47 (1993) 7560–7567.

[29] H. Hijazi, T. Langlinay, H. Rothard, P. Boduch, F. Ropars, A. Cassimi, L.S. Farenzena, E.F. da Silveira, Eur. J. Phys. D 68 (2014) 185.

[30] I.V. Vorobyova, Nucl. Instr. Meth. B 174 (2001) 70–76.

[31] I. Baranov, S. Kirillov, A. Novikov, V. Obnorskii, M. Toulemonde, K. Wien, S. Yarmiychuk, V.A. Borodin, A.E. Volkov, Nucl. Instr. Meth. B 230 (2005) 495–501.

[32] B. Satpati, J. Ghatak, P.V. Satyam, B.N. Dev, J. Appl. Phys. 98 (2005) 064904.

[33] U.B. Singh, D.C. Agarwal, S.A. Khan, S. Mohapatra, A. Tripathi, D.K. Avasthi, J. Phys. D: Appl. Phys. 45 (2012) 45304.

[34] P.K. Kuiri, B. Joseph, H.P. Lenka, G. Sahu, J. Ghatak, D. Kanjilal, D.P. Mahapatra, Phys. Rev. Lett. 100 (2008) 245501.

[35] S. Mohapatra, Appl. Surf. Sci. 283 (2013) 128–133.

[36] G. Greaves, J.A. Hinks, P. Busby, N.J. Mellors, A. Ilinov, A. Kuronen, K. Nordlund, S.E. Donnelly, Phys. Rev. Lett. 111 (2013) 065504.

[37] J.A.M. Pereira, E.F. da Silveira, Nucl. Instr. Meth. B 127–128 (1997) 157–159.

[38] J.A.M. Pereira, E.F. da Silveira, Surf. Sci. 390 (1997) 158–163.

[39] J.A.M. Pereira, E.F. da Silveira, Nucl. Instr. Meth. B 146 (1998) 185.

[40] H. Hijazi, H. Rothard, P. Boduch, I. Alzaher, T. Langlinay, A. Cassimi, F. Ropars, T. Been, J.M. Ramillon, H. Lebius, B. Ban-d'Etat, L.S. Farenzena, E.F. da Silveira, Eur. J. Phys. D 66 (2012) 305.

[41] H. Hijazi, H. Rothard, P. Boduch, I. Alzaher, A. Cassimi, F. Ropars, T. Been, J.M. Ramillon, H. Lebius, B. Ban-d'Etat, L.S. Farenzena, E.F. da Silveira, Eur. J. Phys. D 66 (2012) 68.

[42] W. Assmann, B. Ban-d'Etat, M. Bender, P. Boduch, P.L. Grande, H. Lebius, D. Lelièvre, G.G. Marmitt, H. Rothard, T. Seidl, D. Severin, K.-O. Voss, M. Toulemonde, C. Trautmann, Nucl. Instr. Meth. B 392 (2017) 94–101.

[43] M. Toulemonde, W. Assmann, D. Muller, C. Trautmann, Nucl. Instr. Meth. B 406 (2017) 501–506.

[44] M. Toulemonde, W. Assmann, B. Ban-d'Etat, M. Bender, A. Bergmaier, P. Boduch, S. Della-Negra, J. Duan, A.S. El-Said, F. Grüner, J. Liu, D. Lelièvre, H. Rothard, T. Seidl, D. Severin, J.P. Stoquert, K.-O. Voss, C. Trautmann, Eur. J. Phys. D 74

(2020) 144.

[45] J.F. Ziegler, M.D. Ziegler, J.P. Biersack, 2012. http://www.srim.org.

[46] N. Khalfaoui, C.C. Rotaru, S. Bouffard, M. Tolemonde, J.P. Stoquert, F. Haas, C. Trautmann, J. Jensen, A. Dunlop, Nucl. Instr. Meth. B 240 (2005) 819–828.

[47] R.K. Pandey, M. Kumar, S.A. Khan, T. Kumar, A. Tripathi, D.K. Avasthi, A.C. Pandey, Appl. Surf. Sci. 289 (2014) 77–80.

[48] I. Alencar, J. Ruiz-Fuertes, K. Schwartz, C. Trautmann, L. Bayarjargal, E. Haussühl, B. Winkler, J. Raman Spectrosc. 47 (2016) 978–983.

[49] D. Nečas, P. Klapetek, Cent. Eur. J. Phys. 10 (2012) 181–188.

[50] M. Couprie, G. Bertrand, Proc. SPIE 3168 (1997) 136–146.

[51] P. Klapetek, I. Ohlídal, D. Franta, A. Montaigne-Ramil, A. Bonanni, D. Stifter, H. Sitter, Acta Phys. Slovaca 53 (2003) 223–230.

[52] R.M. Tromp, M. Copel, M.C. Reuter, M.H. von Hoegen, J. Speidell, Rev. Sci. Instr. 62 (1991) 2679–2683.

[53] H. Trombini, G.G. Marmitt, I. Alencar, D.L. Baptista, S. Reboh, F. Mazen, R.B. Pinheiro, D.F. Sanchez, C.A. Senna, B.S. Archanjo, C.A. Achete, P.L. Grande, Sci. Rep. 9 (2019) 11629.

[54] G.G. Marmitt, Metal oxides of resistive memories investigated by electron and ion backscattering, PhD thesis, Universidade Federal do Rio Grande do Sul (2017).

[55] G.G. Marmitt, 2020. http://tars.if.ufrgs.br.

[56] M.A. Sortica, P.L. Grande, G. Machado, L. Miotti, J. Appl. Phys. 106 (2009) 114320.

[57] T. Nishimura, K. Mitsuhara, A. Visikovskiy, Y. Kido, Nucl. Instr. Meth. B 280 (2012) 5–9.

[58] A. Hentz, G.S. Parkinson, P.D. Quinn, M.A. Muñoz-Márquez, D.P. Woodruff, P.L. Grande, G. Schiwietz, P. Bailey, T.C.Q. Noakes, Phys. Rev. Lett. 102 (2009) 096103.

[59] P.L. Grande, A. Hentz, R.P. Pezzi, I.J.R. Baumvol, G. Schiwietz, Nucl. Instr. Meth. B 256 (2007) 92–96.

[60] J.B. Marion, F.C. Young, Nuclear Reaction Analysis: Graphs and tables, North-Holland Publishing Company, 1968.

[61] R.C. Birtcher, S.E. Donnelly, S. Schlutig, Phys. Rev. Lett. 85 (2000) 4968–4971.

[62] L.E. Rehn, R.C. Birtcher, S.E. Donnelly, P.M. Baldo, L. Funk, Phys. Rev. Lett. 87 (2001) 207601.

[63] M. Lawn, R. Goreham, J. Herrmann, A.K. Jämting, J. Micro/Nanolitho. MEMS MOEMS 11 (2012) 011007.

[64] M. Kumar, P. Rajput, S.A. Khan, D.K. Avasthi, A.C. Pandey, Appl. Surf. Sci. 256 (2010) 2199–2204.

[65] H.D. Mieskes, W. Assmann, F. Grüner, H. Kucal, Z.G. Wang, M. Toulemonde, Phys. Rev. B 67 (2003) 155414.

[66] Z. Postawa, M. Szymoński, Phys. Rev. B 39 (1989) 12950–12953.

[67] R. Kelly, J. Chem. Phys. 92 (1989) 5047–5056.

[68] R. Kelly, R.W. Dreyfus, Nucl. Instr. Meth. B 32 (1988) 341–348.

[69] M. Toulemonde, A. Benyagoub, C. Trautmann, N. Khalfaoui, M. Boccanfuso, C. Dufour, F. Gourbilleau, J.J. Grob, J.P. Stoquert, J.M. Costantini, F. Haas, E. Jacquert, K.-O. Voss, A. Meftah, Phys. Rev. B 85 (2012) 054112.

[70] N. Matsunami, M. Sataka, S. Okayasu, M. Tazawa, Nucl. Instr. Meth. B 256 (2007) 333–336.

[71] N. Matsunami, M. Sataka, A. Iwase, S. Okayasu, Nucl. Instr. Meth. B 209 (2003) 288–293.

[72] I.S. Bitensky, E.S. Parilis, Nucl. Instr. Meth. B 21 (1987) 26–36.

[73] H.M. Urbassek, Nucl. Instr. Meth. B 31 (1988) 541–550.

[74] E. Gruber, P. Salou, L. Bergen, M. El Kharrazi, E. Lattouf, C. Grygiel, Y. Wang, A. Benyagoub, D. Lavavasseur, J. Rangama, H. Lebius, B. Ban-d'Etat, M. Schleberger, F. Aumayr, J. Phys.: Condens. Matter 28 (2016) 405001.

[75] N. Ishikawa, T. Taguchi, N. Okubo, Nanotechnol. 28 (2017) 445708.